

Understanding summertime peroxyacetyl nitrate (PAN) formation and its relation to aerosol pollution: Insights from high-resolution measurements and modeling

Baoye Hu^{1,3,4}, Naihua Chen^{1,6}, Rui Li⁷, Mingqiang Huang^{1,3,4}, Jinsheng Chen^{2,5*}, Youwei Hong^{2,5}, Lingling Xu^{2,5}, Xiaolong Fan^{2,5}, Mengren Li^{2,5}, Lei Tong², Qiuping Zheng⁸, Yuxiang Yang^{6*}

¹College of Chemistry, Chemical Engineering and Environment, Minnan Normal University, Zhangzhou, China, 363000

²Center for Excellence in Regional Atmospheric Environment, Institute of Urban Environment, Chinese Academy of Sciences, Xiamen 361021, China

³Fujian Provincial Key Laboratory of Modern Analytical Science and Separation Technology, Minnan Normal University, Zhangzhou, China, 363000

⁴Fujian Province University Key Laboratory of Pollution Monitoring and Control, Minnan Normal University, Zhangzhou, China, 363000

⁵Fujian Key Laboratory of Atmospheric Ozone Pollution Prevention, Chinese Academy of Sciences, Xiamen 361021, China

⁶Pingtang Environmental Monitoring Center of Fujian, Pingtan 350400, China

⁷Key Laboratory of Geographic Information Science of the Ministry of Education, School of Geographic Science, East China Normal University, Shanghai 200241, PR China

⁸Xiamen Key Laboratory of Straits Meteorology, Xiamen Meteorological Bureau, Xiamen 361012, China

Correspondence to: Jinsheng Chen (jschen@iue.ac.cn) & Yuxiang Yang (907460293@qq.com)

Abstract: Peroxyacetyl nitrate (PAN), a key indicator of photochemical pollution, is generated similarly to ozone (O₃), through reactions involving specific volatile organic compounds (VOCs) and nitrogen oxides. Notably, PAN has been observed at unexpectedly high concentrations (maximum: 3.04 ppb) during the summertime. The average daily values of PAN showed a strong correlation with black carbon (BC) (R=0.77) and O₃ (R=0.77), suggesting a close connection between summertime haze and photochemical pollution. We addressed the puzzle of summertime PAN formation and its association with aerosol pollution under high O₃ conditions in Xiamen, a coastal city in southeastern China, by analyzing continuous high temporal resolution data utilizing box modeling in conjunction with the master chemical mechanism (MCM) model. The MCM model, with an index of agreement (IOA) value of 0.75, effectively investigate PAN formation, performing better during the clean period (R²: 0.68, slope K: 0.91) than haze one (R²: 0.47, slope K: 0.75). Using extreme gradient boosting (XGBoost), we identified NH₃, NO₃⁻, and PM_{2.5} as the primary factors for simulation bias. Moreover, the net production rate of PAN becomes negative with PAN constrained, suggesting

删除了: maximum

删除了: er

删除了: 85

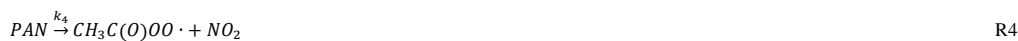
删除了: than with

删除了: 75

35 an unknown compensatory mechanism. Both relative incremental reactivity (RIR) and empirical kinetic modeling approach (EKMA)
36 analyses indicate that PAN formation is VOC-controlled. Controlling emissions of VOCs, particularly alkenes, C₅H₈, and aromatics,
37 would mitigate PAN pollution. PAN promotes OH and HO₂ while inhibiting the formation of O₃, RO₂, NO, and NO₂. This study
38 deepens our comprehension of PAN photochemistry while also offering scientific insights for guiding future PAN pollution control
39 strategies.

41 Introduction

42 PAN is a significant secondary gaseous pollutant commonly present in photochemical smog and poses risk to human health and
43 plant growth, being 1-2 magnitudes more phytotoxic than O₃ (Yukihiro et al., 2012; Taylor, 1969). Additionally, PAN's low aqueous
44 solubility, minimal reactivity with hydroxyl radicals (OH), and slow photolysis contribute to its capacity for long-range transport of
45 nitrogen oxides (NO_x) (Xu et al., 2018; Zhai et al., 2024; Marley et al., 2007b). Therefore, its formation in polluted areas holds
46 significant importance beyond local concerns. Similar to surface O₃, PAN is produced during the oxidation of VOCs in the presence
47 of NO_x (R1-R3) (Xu et al., 2021). PAN is formed when NO₂ reacts with peroxyacetyl (PA) radicals (CH₃C(O)OO·) (R2), but the
48 presence of NO consumes PA radicals, inhibiting PAN production (R3), which creates a comparable dependence of PAN and O₃ on
49 NO and NO₂ levels. Unlike O₃, however, PAN is influenced by only a limited number of oxygenated VOCs (OVOCs) that generate
50 PA radicals. These OVOCs, which are second-generation precursors of PAN, include acetaldehyde (CH₃CHO), acetone
51 (CH₃C(O)CH₃), methylglyoxal (MGLY, CH₃C(O)CHO), methyl vinyl ketone (MVK, CH₂CHC(O)CH₃), methyl ethyl ketone (MEK,
52 CH₃C(O)CH₂CH₃), methacrolein (MACR, CH₂C(CH₃)CHO), and biacetyl (CH₃C(O)C(O)CH₃). These compounds are typically
53 formed from the oxidation of alkenes, aromatics, and isoprene, which are the first-generation precursors of PAN (Xue et al., 2014;
54 Zhang et al., 2015). Identifying the dominant precursors is crucial for managing PAN pollution effectively. In the troposphere,
55 thermal decomposition (R4) is the primary process responsible for PAN loss.



60 In recent years, wintertime photochemical air pollution has increasingly garnered attention. At this time, the concentration of O₃ is
61 low due to the strong titration of NO, while the concentration of aerosol is high, and it is found that aerosol promotes PAN generation
62 (Xu et al., 2021). Surprisingly high concentrations of OH radical, particularly under hazy conditions, have been observed and are
63 largely attributed to HONO photolysis (Xu et al., 2021). Winter photochemical and haze pollution often exacerbate each other, with
64 photochemical trace gases supplying both oxidants and precursors for aerosol formation, and aerosols acting as mediums for

删除了: •

66 heterogeneous reactions that produce key oxidants such as HONO, H₂O₂, and OH radicals (Xu et al., 2021). The OH produced by
67 HONO photolysis can partially replace the UV action to promote PAN formation in winter in southeast coastal area of China when
68 particulate matter is high ($\geq 35 \mu\text{g}\cdot\text{m}^{-3}$) (Hu et al., 2020). Zhang et al. (2020) found the potential HONO sources significantly
69 improved the PAN simulations in wintertime heavy haze events with high concentrations of PAN. High concentrations of PAN are
70 a consequence of the increased levels of precursors and HONO observed during haze episodes (Liu et al., 2018). In conclusion,
71 most previous studies have studied the effect of aerosol on PAN generation in winter. Further research on PAN should determine
72 whether particulates significantly contribute to its formation during warmer seasons with elevated O₃ concentrations (Xu et al.,
73 2021). In Eastern China, photochemical air pollution often involves high concentrations of both O₃ and PAN, a persistent issue
74 during the warm season (April-September) for many years (Lu et al., 2020). The characteristics and formation pathways of PAN
75 during summer have been increasingly studied in regions such as the North China Plain (NCP), the Yangtze River Delta, the Pearl
76 River Delta, and southwestern China. These studies have generally shown consistent diurnal patterns and strong correlations
77 between PAN and O₃, identifying acetaldehyde—primarily derived from the degradation of aromatics and alkenes—as the key direct
78 precursor of PAN in the summer. However, there has been limited research on the formation of PAN and its relationship with aerosol
79 pollution during the summertime.

80 Xiamen is one of the fastest urbanizing regions in the southeast China and is also one of the cities with the best air quality in China,
81 where the air quality could represent the future of other Chinese urban regions. Between 2018 and 2023, Xiamen ranked among the
82 top 10 cities in China, achieving positions of 7th in 2018, 4th in both 2019 and 2020, 6th in 2021, 9th in 2022, and returning to 7th
83 in 2023 (mee.gov.cn, last assessed October 30, 2014). Xiamen is located in a low-latitude coastal area, with abundant sunlight and
84 long daylight hours during the summer, resulting in strong solar radiation and rapid photochemical conversion rates. The city is
85 typically influenced by the East Asian monsoon and serves as a transport channel for atmospheric pollutants from both the Yangtze
86 River Delta and Pearl River Delta regions. Additionally, during the summer, Xiamen is often affected by complex meteorological
87 conditions such as typhoons and the West Pacific Subtropical High (WPSH). The WPSH creates weather conditions that promote
88 the formation and accumulation of photochemical pollutants and particulate matter (Wu et al., 2019). This setting provides an ideal
89 "laboratory" for investigating the complexities of summertime PAN formation and its relationship with aerosol pollution under high
90 O₃ concentrations. In summer, especially in July, high temperatures, high humidity, and intense radiation are likely to accelerate
91 both the formation and consumption rates of PAN. In this study, continuous measurements of trace gases, substances related to
92 aerosols, photolysis rate constants and meteorological parameters were performed at a suburban site in Xiamen from ~~10 to 31 July~~,
93 2018. Firstly, we provide an overview of pollutant concentrations, meteorological parameters, and weather conditions during the
94 observation period. Secondly, we simulate PAN concentration with the aid of box modeling combined with master chemical
95 mechanism (MCM) ~~model~~. Using machine learning with XGBoost, we identified the key factors that affect the observation-based
96 model (OBM) model's simulation results and clarified the mechanisms linking haze pollution to photochemical air pollution, as

删除了: July 10th

删除了: 31st.

99 indicated by PAN and O₃. Thirdly, the study identified the main precursors and oxidants responsible for summertime PAN production
100 in Xiamen and evaluated the influence of PAN on local atmospheric oxidation capacity. This study further emphasized the interplay
101 between haze and photochemical air pollution and highlighted significant implications for future research.
102

103 2 Methodology

104 2.1 Field observations

105 Trace gases (including PAN, O₃, HONO, HNO₃, HCl, NH₃, VOCs, NO_x, CO, and SO₂), substances related to aerosols (including
106 BC, PM₁, PM_{2.5}, PM₁₀, SO₄²⁻, NO₃⁻, NH₄⁺, Cl⁻, Na⁺, K⁺, Ca²⁺, Mg²⁺), photolysis rate constants (including JO¹D, JNO₂, JHONO,
107 JHCHO_M, JHCHO_R, JNO₃_M, JNO₃_R, JH₂O₂), and meteorological parameters (including temperature, relative humidity,
108 atmospheric pressure, wind speed, and wind direction) were continuously measured at a suburban site in Xiamen from 10 to 31
109 July 2018. All instruments were placed inside an air-conditioned container situated on the rooftop of a 20-story building at the
110 Institute of Urban Environment, Chinese Academy of Sciences (IUE: 118.06°_E, 24.61°_N) (Fig. S1(a)). When southerly winds
111 prevailed, Xiamen Island, characterized by dense population and traffic congestion, was located upwind of the IUE (Fig. S1(b)).
112 The IUE supersite is surrounded by Xinglin Bay, several universities and institutes, and major roadways with heavy traffic, such as
113 Jimei Road (< 200 m), Shenhai Expressway (870 m), and Xiasha Expressway (2300 m) (Fig. S1(c)).

114 PAN measurements were conducted using a PANS-1000 analyzer (Focused Photonics Inc., Hangzhou, China), which features an
115 automated system consists of a gas chromatograph, an electron capture detector, and a calibration unit. The analyzer provided PAN
116 readings every 5 minutes, with a detection limit of 50 ppt. The uncertainty and precision of the PAN measurements were ±10% and
117 3%, respectively. The PAN standard gas was produced through the reaction of acetone and NO under UV light. Calibration
118 procedures included monthly multi-point calibrations and weekly single-point calibrations. Detailed information about the PAN
119 detection system and calibration can be found in previous studies (Hu et al., 2020; Liu et al., 2022a). The VOC measurements were
120 conducted using a gas chromatography mass spectrometer (GC-FID/MS, TH-300B, Wuhan, China) at an hourly time resolution.
121 Detailed information regarding the VOC detection system and calibration procedures is available in our previous study (Liu et al.,
122 2022b). HONO measurements were conducted using a customized Incoherent BroadBand Cavity Enhanced Absorption
123 Spectroscopy (IBBCEAS) system developed by the Anhui Institute of Optics and Fine Mechanics (AIOFM), Chinese Academy of
124 Sciences. The HONO detection limit was 100 ppt, with a time resolution of 1 minute. The measurement principle and calibration
125 method of IBBCEAS can be found in the previous literature (Hu et al., 2022; Duan et al., 2018; Hu et al., 2024). The concentrations
126 of inorganic components in PM_{2.5} aerosols (including SO₄²⁻, NO₃⁻, NH₄⁺, Cl⁻, Na⁺, K⁺, Ca²⁺, Mg²⁺), as well as the concentrations of
127 gases such as NH₃, HCl, and HNO₃ were analyzed using a Monitor for AeRosols and Gases in ambient Air (MARGA, Model ADI
128 2080, Applikon Analytical B.V., the Netherlands) (Hu et al., 2022). The criteria air pollutants O₃, NO_x, CO, and SO₂ were measured
129 using different methods: ultraviolet (UV) absorption for O₃ (TEI model 49i), chemiluminescence with a molybdenum converter for

删除了: July 10th to July 31st, 2018

131 NO_x (TEI model 42i), non-dispersive infrared for CO (TEI model 48i), and pulsed UV fluorescence for SO₂ (TEI model 43i). A
132 tapered element oscillating microbalance (TEOM1405, Thermo Scientific Corp., MA, USA) was used to continuously measure the
133 mass concentrations of PM₁, PM_{2.5}, and PM₁₀ online. A photolysis spectrometer (PFS-100, Focused Photonics Inc., Hangzhou,
134 China) was employed to measure the photolysis rate constants. An ultrasonic anemometer (150WX, Airmar, USA) was used to
135 measure meteorological parameters.

136

137 **2.2 Box modeling**

138 This study employed a box model framework utilizing the Master Chemical Mechanism (MCMv3.3.1,
139 <https://mcm.york.ac.uk/MCM/home.htm>) to investigate sensitivity and mechanisms of PAN formation. The model constraints were
140 derived from observations of trace gases and meteorological parameters, which were averaged to 1-hour intervals. The reliability of
141 model simulation results is often assessed using the index of agreement (IOA), which ranges from 0 to 1, with a higher IOA
142 signifying greater alignment between observed and simulated values. Note that the model simulation values at this time are not
143 constrained by PAN. For specific formulas, please refer to the supplementary information (Eq. S1). Other formulas, including PAN
144 production rates (P(PAN)), net production of PAN (Net (PAN)), and the RIR, are provided in the supplementary information (Eq.
145 S2- Eq. S4).

146 The MCM simulates the nonlinear interaction between PAN and its precursors by altering the VOCs-to-NO_x ratio across multiple
147 scenarios, while keeping all other parameters fixed. In this study, a 20% step size was applied, reducing VOCs and NO_x from 200%
148 down to 0% to construct a scenario matrix. A total of 121 scenarios were generated to model the PAN production rate. The scenario
149 representing the average VOCs and NO_x mixing ratio during the sampling period was designated as the base case, with the remaining
150 120 scenarios created by systematically adjusting the VOC-to-NO_x ratio. The output from these 121 simulations was used to
151 construct isopleth diagrams depicting the relationship between VOCs, NO_x, and PAN.

152 **2.3 Machine Learning Model**

153 To identify the key factors influencing the performance of the model simulation, the Machine Learning (ML) model was applied to
154 establish the prediction model of bias between simulation of OBM and observation. XGBoost is a supervised boosting algorithm
155 that reduces the risk of over-fitting, captures the nonlinear relationships among predictor variables, and solves numerous data science
156 problems in a rapid and accurate way (Li et al., 2024). It has demonstrated high performance in O₃ studies in China. As compared
157 to other bagging tree models like random forest, XGBoost can handle more complex data while consuming fewer computing
158 resources. To further improve the interpretability of the ML model, the feature importance of independent input variables in the
159 XGBoost model is quantified using the Shaply Additive explanation (SHAP) approach (Lin et al., 2024). The SHAP calculates a
160 value that represents the contribution of each feature to the model's outcome, which has been successfully applied in atmospheric
161 environmental studies (Li et al., 2024; Lin et al., 2024). When the model was being adjusted, 90% of the data was used as the

删除了: over

163 training [data](#) set, and 10 % of the data was used as the test [data](#) set. The hyperparameters were tuned using grid search and cross-
164 validation method. Specifically, for a single hyperparameter, grid search was used to obtain its more appropriate value range, and
165 for the combinations of hyperparameters, the whole training set was split into ten folds and then run a grid search over pre-adjusted
166 combinations of hyperparameters by training nine folds and predicting on the one [fold](#) in cross-validation procedure. For key
167 hyperparameters of XGBoost model, the number of trees was 100, learning rate was 0.1, max depth was 6. The model was trained
168 and tested on hourly data during the whole observation and the established model was examined by coefficient of determination (R^2)
169 value, the root-mean-squared error (RMSE) and mean absolute error (MAE). The formulas of RMSE and MAE are provided in the
170 supplementary information (Eq. S5 & Eq. S6). The performance of both models is illustrated in Fig. S3. The R^2 , MAE, and RMSE
171 for the training set are 0.90, 0.08, and 0.12, respectively, while the corresponding values for the test set are 0.77, 0.10, and 0.14,
172 respectively. These statistical metrics indicate that the XGBoost model is promising for further analysis.

删除了:

174 3. Results and discussion

175 3.1 Overview of observation

176 The measured data of PAN, related trace gases and meteorological parameters at IUE over [10 to 31 July 2018](#), are documented in
177 Fig. 1. Combined with the synoptic situation shown in Fig. S4, the 8th typhoon of 2018, Typhoon Maria, made landfall on the
178 morning of the 11th at Huangqi Peninsula in Lianjiang County, Fujian. Due to the influence of the typhoon's outer spiral rain bands,
179 there was moderate to heavy rain on the [11 July 2018](#). Correspondingly, there was a noticeable decrease in ultraviolet radiation and
180 the temperatures. Starting from the [12 July 2018](#), a WPSH strengthened and extended westward, exerting control over Xiamen. In
181 the lower atmosphere, it was influenced by the eastward flow, resulting in predominantly cloudy weather. From the [16 to 18 July](#)
182 [2018](#), the area was affected by the outer periphery of Typhoon Shan Shen, which formed on the [17 July 2018](#), in the northeastern
183 part of the South China Sea and moved westward, making landfall along the coast of Wancheng Town, Wanning City, Hainan
184 Province in the early hours of the [17 July 2018](#). During this period, the city experienced strong winds with gusts reaching 5 to 6 on
185 the Beaufort scale in the urban areas. At the same time, the concentration of various pollutants reached their lowest levels, and the
186 daily variation patterns were less pronounced. From the [20 to 21 July 2018](#), Xiamen experienced the influence of the peripheral
187 descending airflow associated with Typhoon Ampil (which formed in the northwest Pacific Ocean around 8:00 [PM local time \(LT\)](#))
188 on the [18 July 2018](#), and moved northwest, making landfall along the coast of Chongming Island, Shanghai, around noon on the [22](#)
189 [July 2018](#)). During this period, there were fewer clouds and higher temperatures. From the [22 to 24 July 2018](#), the city was
190 successively affected by the outer periphery of Typhoon Ampil and a tropical low-pressure system, resulting in occasional showers
191 or thunderstorms. From the [25 to 31 July 2018](#), a WPSH once again strengthened and controlled Xiamen. As a result, Xiamen
192 experienced stable meteorological conditions, with light winds ($w_s = 1.04 \text{ m/s}$), persistently high temperatures (maximum daily
193 average of $37.82 \text{ }^\circ\text{C}$), and high relative humidity (maximum daily average of 81.65%). These factors created an environment that

删除了: 10-31 July 2018

删除了: 11th

删除了: 12th

删除了: 16th to the 18th

删除了: 17th

删除了: 18th

删除了: 20th to the 21st

删除了: P.M.

删除了: 18th

删除了: 22nd

删除了: 22nd to the 24th

删除了: 25th to the 31st

删除了: .

208 favored the buildup of particulate matter and enhanced the photochemical formation of O₃ and PAN (Wu et al., 2019). The maximum
209 daily average of PM_{2.5}, O₃ and PAN were 49.26 μg.m⁻³, 93.62 ppb, and 1.37 ppb, respectively.
210 The phenomenon of simultaneous high levels of photochemical and particulate matter appears. Throughout the 22-days campaign,
211 12 days (including 11, 13, 21, 23, and 25-31 July 2018) were observed with 1 h concentrations of PM_{2.5} exceeding 35 μg.m⁻³; 13
212 days (including 11, 13, 15, 20, 23, and 26-31 July 2018) were observed with 5-min concentrations of PAN exceeding 1 ppb. The
213 maximum concentration was recorded at 3.04 ppb (5-min data) at 11:09 LT of 13 July 2018. This concentration of PAN is comparable
214 to the levels recorded at downwind of Guangzhou, southern China (3.9 ppb, Wang et al., 2010), 2.51 ppb in Nashville, U.S (Roberts
215 et al., 2002). However, this value was significantly lower than heavily polluted areas in northern China in the summer, such as
216 Beijing (9.34 ppb, Xue et al., 2014), Lanzhou (9.12 ppb, Zhang et al., 2009), and Jinan (13.47 ppb, Liu et al., 2018). This is likely
217 because the higher summer temperatures in the southeastern coastal region are conducive to the thermal decomposition of PAN, and
218 the precursor concentrations of PAN, including NO₂ and VOCs, are significantly lower in the studied area compared to those in the
219 northern region. The concentration of alkanes is the highest, followed by alkenes, OVOCs and aromatics, while halogenated
220 hydrocarbons and C₅H₈ exhibit lower concentrations (Fig. S5). Furthermore, VOC concentrations for various species are elevated
221 during haze periods compared to clean periods (Fig. S5). Table S1 provides the detailed VOC concentrations observed during the
222 study period. Throughout the observation period, the variations in O₃ and PAN were almost identical, but the maximum
223 concentration of O₃ occurred at 3:00 PM LT on 29 July 2018 (114.12 ppb). The correlation between the average daily values of PAN
224 and both BC and O₃ is strong, with a correlation coefficient of 0.77 for each (Fig. S6), suggesting that summertime haze and
225 photochemical pollution were deeply connected.

- 删除了: July
- 删除了: th
- 删除了: th
- 删除了: st to
- 删除了: 23rd
- 删除了: 25th
- 删除了: to
- 删除了: st
- 删除了: .
- 删除了: July
- 删除了: th
- 删除了: th
- 删除了: th
- 删除了: th to
- 删除了:
- 删除了: rd
- 删除了: th to
- 删除了:
- 删除了: st
- 删除了: local time
- 删除了:) (
- 删除了: (
- 删除了:)
- 删除了: p.m.
- 删除了: 29th
- 删除了: The correlation between the maximum daily values of PAN and BC is the strongest (R=0.85), followed by O₃ (R=0.75) ...
- 设置了格式: 下标

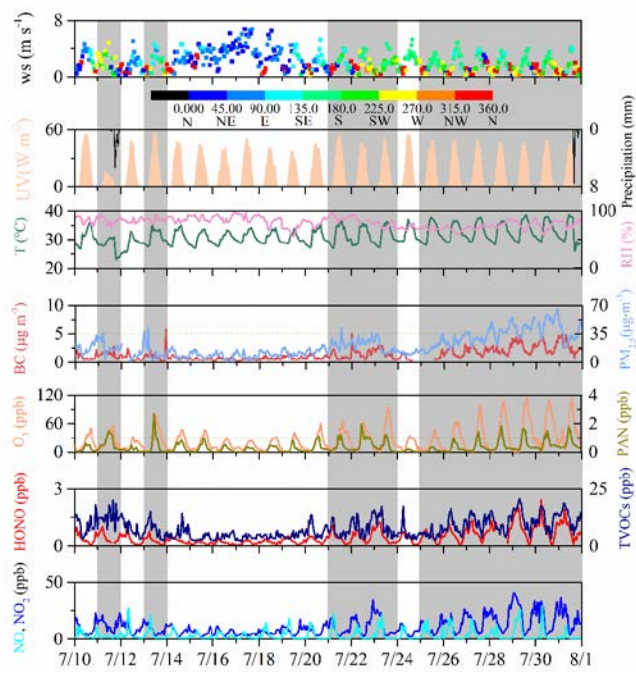
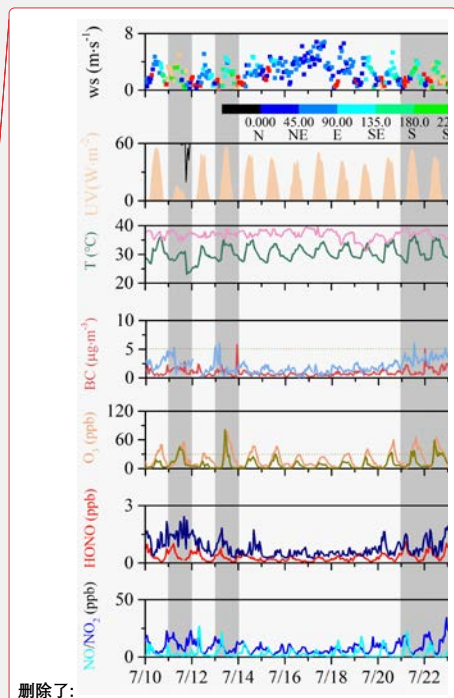


Figure 1. Time series of trace gases and meteorological parameters observed at IUE during 10-31 July 2018. The gray shading represents days when the PM_{2.5} hourly daily maximum value exceeded 35 $\mu\text{g m}^{-3}$.

We categorize it as "haze" and "clean" based on whether the PM_{2.5} hourly daily maximum value is greater than 35 $\mu\text{g m}^{-3}$. Specifically, "haze" includes 11, 13, 21-23, and 25-31 July 2018, while other days are categorized as 'clean'. To provide a quantitative perspective, the statistics for PAN and associated species were calculated and compiled in Table 1. PM_{2.5} concentrations during the haze period were significantly higher than those during the clean period, being 2.49 times those of the clean period. There was no significant difference of UV levels between clean and haze periods, while temperatures in the haze phase were notably higher than those in the clean phase. Therefore, without considering precursors, PAN concentrations should be lower during the haze phase due to higher thermal decomposition. In fact, PAN concentrations during the haze period were 2.35 times higher than those during the clean period. During the haze period, O₃ concentrations were also significantly higher than those during the clean period, being 2.04 times those of the clean period. These observations indicate that the atmospheric oxidation capacity is relatively strong during the haze period. Similar to PAN, HONO also exhibits higher concentrations during the haze phase (approximately 2.33 times that of clean conditions), which is consistent with current research findings that particles promote the generation of HONO (Ye et al., 2017). NO also experienced an increase from clean (3.28 ppb) to hazy (4.30 ppb) conditions, albeit less prominently than NO₂ (from 7.21 to 14.55 ppb). This observation further underscores that, during hazy periods, the



删除了:

删除了: .

删除了: .

删除了: July 11th, 13th, 21st to 23rd, and 25th to 31st

319 12:00 LT caused by thermal decomposition of PAN at high temperatures (Fig. 2). Although PAN and O₃ exhibit a slight bimodal
320 pattern during the clean period, this is primarily due to the bimodal pattern of UV during this time. The peak occurring at noon
321 indicates that PAN primarily originates locally, as a delay of about 1-2 hours would be expected if it were influenced by
322 transportation (Liu et al., 2024). The daytime increment was much larger for hazy condition (1.17 ± 0.44 ppb) than for clean
323 condition (0.52 ± 0.21 ppb), indicating stronger photochemical production of PAN for hazy condition. The daily variation pattern
324 of O₃ is similar to PAN, except that O₃ reaches its peak relatively later compared to PAN, with the peak occurring at 16:00 during
325 the clean phase and 14:00 LT during the haze phase. Although PAN and O₃ are both products of photochemical reactions involving
326 NO_x and VOCs, their production efficiencies differ. PAN is specifically formed from VOCs that are precursors to the acetyl radical
327 (CH₃CO), whereas O₃ can be produced from the oxidation of any VOCs. Analyzing the correlation between PAN and O₃ can offer
328 insights into their respective photochemical production efficiencies. As shown in Fig. S7, the positive correlation between the daily
329 maximum values of PAN and O₃ for clean condition ($R^2=0.67$) was better than that for hazy condition ($R^2=0.15$). The slopes of
330 the linear regression were 0.021 ppb/ppb for clean conditions and 0.009 ppb/ppb for hazy conditions. This indicates that, on average,
331 approximately 2.1 ppb of PAN could be produced for each 100 ppb of O₃ formed under clean conditions, and about 0.9 ppb of
332 PAN for each 100 ppb of O₃ under hazy conditions in the air masses reaching IUE. The slope of linear regression for clean condition
333 is comparable to those determined in Hongkong (0.028, Xu et al., 2015), Mexico city (0.020, Marley et al., 2007a), and Nashville
334 (0.025, Roberts et al., 2002). The lower efficiency of PAN production relative to O₃ indicates that PAN precursors represent only
335 a small portion of the total VOCs, especially during hazy conditions. Additionally, the high temperatures in the southeast coastal
336 region likely contribute to the lower production efficiency of PAN. The average temperature during the entire observation period
337 was 31.39 °C, with an average temperature of 34.64 °C at 12:00 LT. This result is consistent with the result that RIR during the
338 cleaning period is higher than that during the haze period. As shown in Fig. S8, in the clean period, the correlation between PAN
339 and O₃ is the strongest ($R^2=0.70$), indicating that O₃ and PAN are both photochemical end products during clean periods. In contrast,
340 during hazy periods, the correlation between PAN and O₃×JO¹D is the strongest ($R^2=0.66$), suggesting that O₃ plays a more
341 significant role in promoting PAN formation through photolysis to generate OH during hazy periods.

342 Unlike the daily variation patterns of PAN and O₃, HONO exhibits a swift concentration decrease after sunrise in both clean and
343 hazy conditions, undergoing photolytic conversion into OH radicals. Subsequently, in clean conditions, HONO starts to increase
344 in concentration after sunset. In hazy conditions, however, the increase begins from 16:00 LT and not after sunrise. This suggests
345 a robust daytime net production or transport of HONO, where the rates surpass those of HONO photolysis and other sinks in the
346 afternoon in hazy conditions. The NO levels reach their peak at 7:00 LT during the morning rush hour, reflecting advection of fresh
347 urban plumes to the study site. The daily variation of NO₂ exhibits a 'U' shape, reaching its minimum value at 13:00 LT, mainly
348 owing to effects of emission, boundary layer height and photochemical reactions. In the clean period, the daily variation of PM_{2.5}
349 is similar to that of NO₂, both showing a 'U' shape, reaching their lowest values at noon. However, during the haze phase, the daily

删除了: 01

删除了: 04

删除了: (

删除了:)

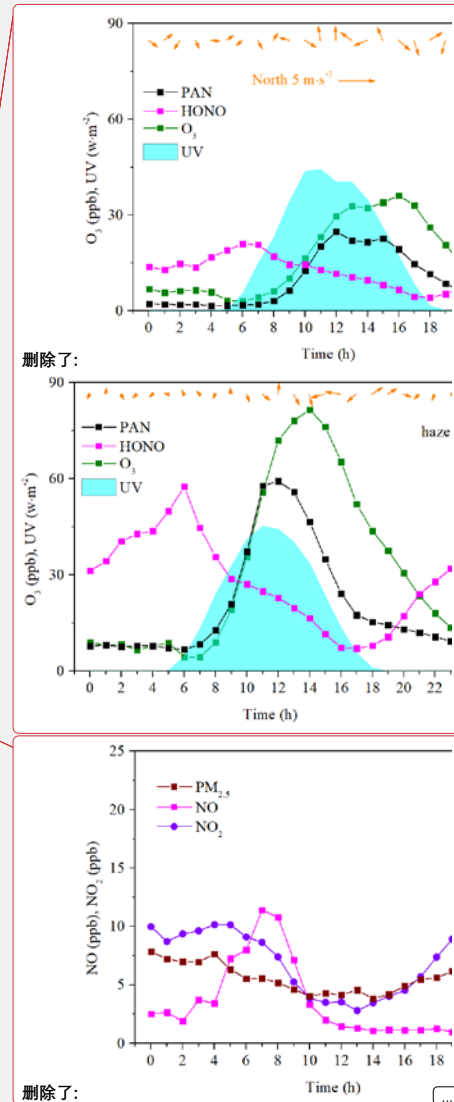
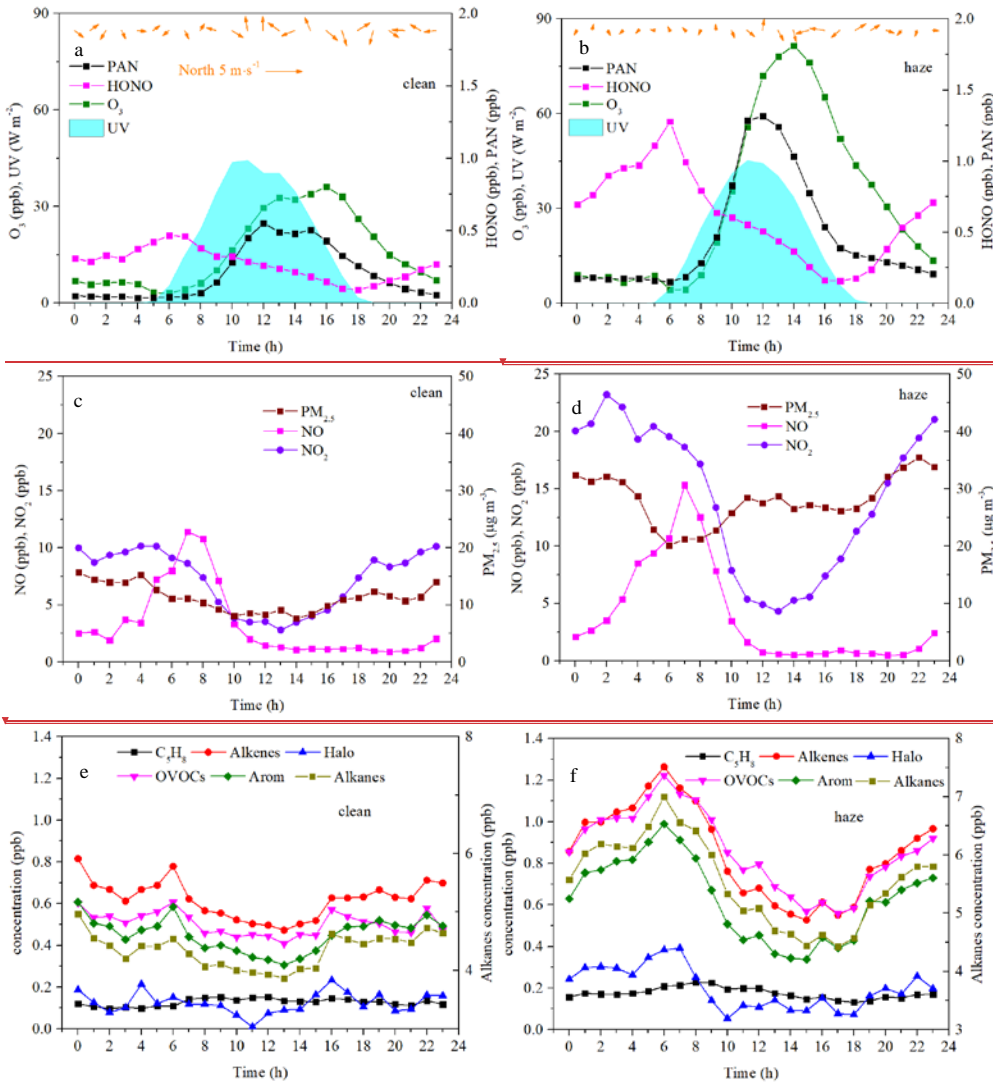
删除了: (

删除了:)

删除了: (

删除了:)

358 variation pattern of $PM_{2.5}$ appears somewhat different. There is a noticeable trough in the early morning, remains stable during the
 359 day, and starts to rise after sunset. The diurnal variation of VOC concentrations for various species are not significant during clean
 360 periods (Fig. 2(e)), likely due to higher wind speeds that facilitate the dispersion of pollutants. In contrast, during haze periods, the
 361 daily variations are evident, with peaks occurring before sunrise, followed by a decline, and then an increase after sunset (Fig.
 362 2(f)). This is because the haze period is relatively stable at nighttime, which allows for the accumulation of pollutants, while during
 363 the daytime, sunlight converts VOCs into photochemical products like O_3 and PAN.



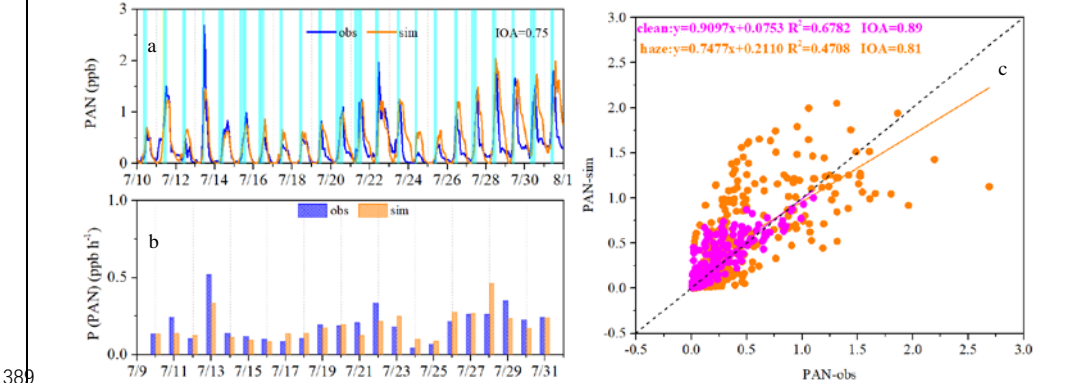
366 **Figure 2.** The diurnal variations of PAN, HONO, O_3 , and UV during clean (a) and hazy (b) periods, the diurnal variations of $PM_{2.5}$,
 367

373 NO, and NO₂ during clean (c) and hazy (d) periods, and the diurnal variations of isoprene (C₅H₈), Alkenes, halogenated
374 hydrocarbons (Halo), OVOCs, aromatics (Arom), and alkanes during clean (e) and hazy periods (f).

375

376 3.2 PAN formation: key factors and mechanisms

377 To investigate the key factors and mechanisms of PAN formation, PAN was simulated by constraining the MCM-based box model
378 with meteorological conditions and observed concentrations of precursor gases. The model successfully replicated the variations
379 in PAN, achieving an IOA of 0.75 (Fig. 3(a)), which was within the accepted range (0.66-0.87) in previous studies (Zeng et al.,
380 2019). The model captured its formation rate in general well, with observed rates varying from 0.04 to 0.52 ppb·h⁻¹ (average: 0.20
381 ppb·h⁻¹) and modeled rates ranging from 0.09 to 0.46 ppb·h⁻¹ (average: 0.19 ppb·h⁻¹) (see Fig. 3(b)). The similar result was found
382 in the North China Plain (NCP) region in the wintertime (Xu et al., 2021). When calculating the IOA separately for clean and hazy
383 periods, it was found that the IOA significantly increased to 0.89 and 0.81 (Fig. 3(c)), respectively. This phenomenon indicates a
384 substantial difference in the PAN production and destruction mechanisms between clean and hazy periods. Furthermore, the
385 simulated values are closer to the observed values during clean period, reflected in a higher R² value (R²=0.68) and a slope value
386 (K) closer to 1 (K=0.91) (Fig. 3(c)). In contrast, the R² value and the K value during hazy period are only 0.47 and 0.75, respectively
387 (Fig. 3(c)). This phenomenon suggests that some reactions related to PAN generation or destruction might be missing in the MCM
388 during the hazy period.

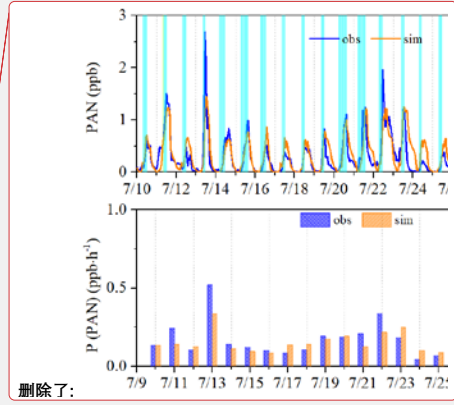


390 **Figure 3.** Comparisons of observed (obs) PAN and simulated (sim) PAN (daytime photochemical PAN production periods
391 indicated by cyan shading), (b) production rates, (c) correlation between PAN observations and simulated values.

392

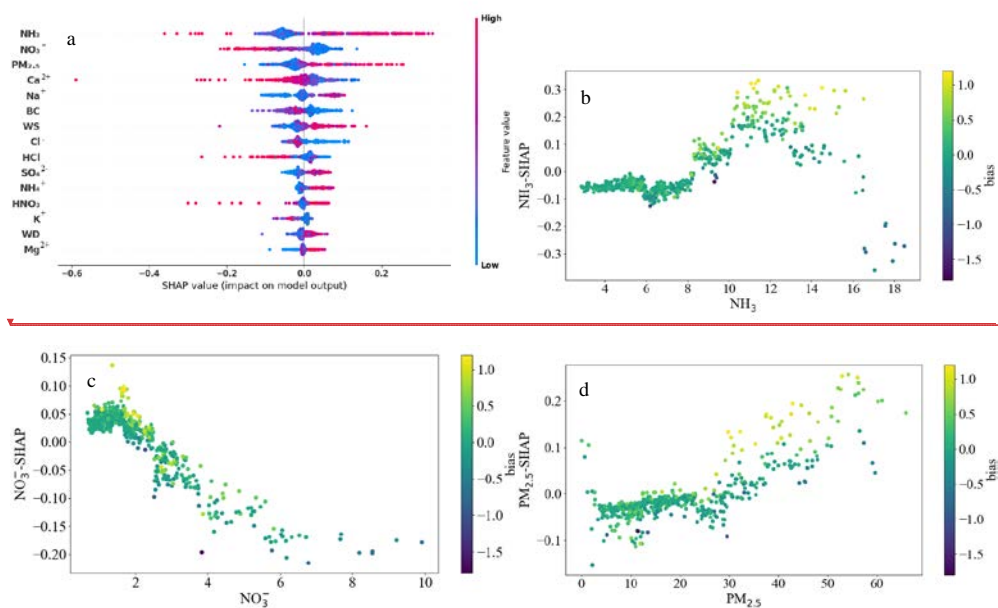
393 To identify the key factors influencing the performance of the OBM model simulation, the bias (the model simulation minus the
394 observed value) as the target. The remaining variables, which were not input into the OBM model, such as NH₃, HNO₃, HCl
395 (alkaline and acidic gaseous pollutants), PM_{2.5} concentrations and their components, as well as physical process parameters like
396 wind speed and wind direction, were used as features. As shown in Fig. 4 (a), through XGBoost-SHAP machine learning, we found

删除了: .
删除了: in general



删除了:

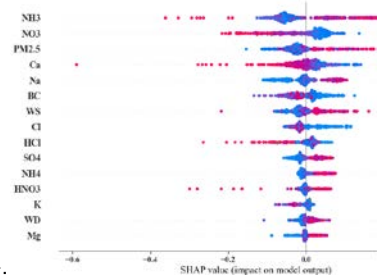
400 that NH_3 is the most significant parameter affecting bias, contributing 19.68 % (Fig. S9). A scatter plot analysis of the SHAP values
 401 of NH_3 versus NH_3 concentrations revealed that as NH_3 concentrations increase (Fig. 4 (b)), the OBM model tends to overestimate
 402 PAN concentration more significantly. To date, there are very few studies that directly address the impact of NH_3 on PAN formation.
 403 Xu et al. (2021) suggested that NH_3 could promote the formation of HONO, which in turn affects PAN formation. However, since
 404 we included HONO as an input to constrain the model, the indirect influence of NH_3 on PAN formation through HONO can be
 405 excluded. NH_3 in the atmosphere can preferentially react with sulfuric acid (H_2SO_4) to form ammonium sulfate ($(\text{NH}_4)_2\text{SO}_4$)
 406 secondary inorganic aerosols (Behera et al., 2013), leading to the heterogeneous reaction removal of PAN by secondary inorganic
 407 aerosols (Pratap et al., 2021). This result is validated by the positive correlation between the SHAP values of NH_4^+ and SO_4^{2-} and
 408 their respective concentrations (Fig. S10). NO_3^- is the second most significant parameter influencing the bias between the two,
 409 contributing 11.33 % (Fig. S9). NO_3^- has a negative correlation with the bias (Fig. 4 (c)), indicating that higher NO_3^- levels lead to
 410 more significant underestimation by the model. Considering the significant positive correlation between PAN and NO_3^- at the 0.01
 411 level, with a correlation coefficient of 0.37, and the fact that both reach their peaks around noon (Fig. S11), it is likely that they
 412 have a common source. $\text{PM}_{2.5}$ is the third most significant parameter (Fig. 4 (a)), contributing 9.40 % (Fig. S9). $\text{PM}_{2.5}$ has a positive
 413 correlation with the bias (Fig. 4 (d)), indicating that higher $\text{PM}_{2.5}$ levels lead to more significant overestimation by the model,
 414 suggesting that PAN can undergo heterogeneous removal on the surface of $\text{PM}_{2.5}$ in the actual atmosphere (Sun et al., 2022).



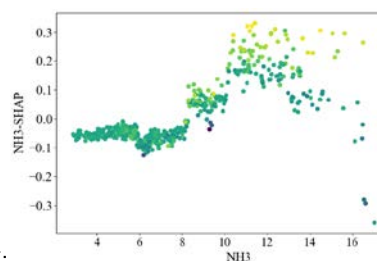
417 **Figure 4.** Feature importance was obtained by XGBoost-SHAP method (a). The scatter plots between concentration of top three
 418 important features and their SHAP values (b, c and d), and colored with the bias (the model simulation minus the observed value).

删除了: (

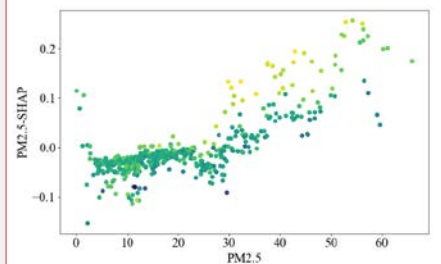
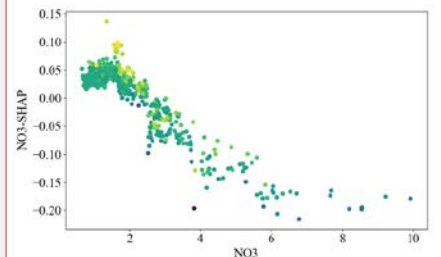
删除了:)



删除了:



删除了:



425

426 Figure 5 (a) and (b) show the average production and destruction rates of PAN during clean and haze periods, as simulated by
 427 OBM without PAN constrained. During the haze period, both the production and destruction rates of PAN are significantly higher
 428 than during the clean period. The higher production rate of PAN during the haze period is due to the higher concentration of PAN
 429 precursors, while the higher destruction rate is because both the temperature and PAN concentration are higher. Regarding the net
 430 production rate, it is also higher during the haze period than during the clean period, which corresponds to the previously observed
 431 diurnal variation. From 6:00 to 12:00 LT during the haze period, the simulated net production rate of PAN is positive, with an
 432 average value of 0.19 $\text{ppb}\cdot\text{h}^{-1}$. During the clean period, from 6:00 to 12:00 LT, the simulated net production rate of PAN is 0.12
 433 $\text{ppb}\cdot\text{h}^{-1}$. The observed diurnal variation of PAN shows that from 6:00 to 12:00 LT, the average net production rates during the haze
 434 and clean periods are 0.20 $\text{ppb}\cdot\text{h}^{-1}$ (Fig. 2(a)) and 0.09 $\text{ppb}\cdot\text{h}^{-1}$ (Fig. 2(b)), respectively. The model-simulated net production rate is
 435 close to the observed net production rate, further indicating that the model can simulate PAN well, and also confirming that PAN
 436 in summer mainly comes from local production. The net production rate of PAN during the haze period is similar to the summer
 437 results in urban areas of the Pearl River Delta (PRD), which is 0.17 $\text{ppb}\cdot\text{h}^{-1}$, while the net production rate of PAN during the clean
 438 period is similar to the summer results in rural areas of the PRD, which is 0.12 $\text{ppb}\cdot\text{h}^{-1}$ (Liu et al., 2024).

439 Figure 5 (c) and (d) show the average production and destruction rates of PAN during clean and haze periods, as simulated by OBM
 440 with PAN constrained. The net production rate of PAN is approximately zero at night during both clean and haze periods, while
 441 there is a significant difference in the net production rate during the day. During the clean period, the daytime net production rate of
 442 PAN is greater than zero, with an average value of 0.19 $\text{ppb}\cdot\text{h}^{-1}$. In contrast, during the haze period, the net production rate of PAN
 443 is negative from 6 AM to 1 PM LT, with an average value of -0.47 $\text{ppb}\cdot\text{h}^{-1}$, and positive from 2 PM to 5 PM LT, with an average
 444 value of 0.47 $\text{ppb}\cdot\text{h}^{-1}$. Previous research has shown that an increase in temperature, an increase in PAN concentration, or a decrease
 445 in PAN precursors (including VOCs and NO_2) can cause the net production rate of PAN to change from positive to negative (Liu et
 446 al., 2024). We conducted a correlation analysis of the net production rate of PAN with temperature, PAN, VOCs, and NO_2
 447 concentration and found that the net production rate of PAN had the best correlation with PAN concentration ($R^2=0.13$), showing a
 448 significant negative correlation ($k=-0.53$, Fig. S12). Additionally, we also observed that when the net production rate of PAN is
 449 negative, the PAN concentration is often very high (Fig. S12). As shown in Fig. 6, we conducted sensitivity experiments by reducing
 450 the PAN concentration by 80 %, i.e., 0.2 times the observed value, and found that the simulated net production rate of PAN was
 451 positive throughout the observation period. Conversely, when the PAN concentration was increased by 140 %, i.e., 2.4 times the
 452 observed value, the simulated net production rate of PAN was found to be almost negative throughout the observation period.
 453 Besides, we also conducted sensitivity experiments on temperature and found that when simulating winter temperatures, i.e., 0.4
 454 times the observed value, with a temperature range of 9.25-15.29 $^\circ\text{C}$, the simulated net production rate of PAN was positive
 455 throughout the observation period. Similarly, when simulating spring and autumn temperatures, i.e., 0.6 times the observed value,

删除了: .

删除了: a.m.

删除了: p.m.

删除了: .

删除了: p.m.

删除了: p.m

删除了: .

删除了: .

删除了: 16

删除了: 5283

删除了:) (

with a temperature range of 13.87-23.39 °C, the simulated net production rate of PAN was also positive throughout the observation period. In conclusion, the simulated net production rate of PAN becomes negative with PAN constrained, further suggesting the existence of an unknown compensatory mechanism.

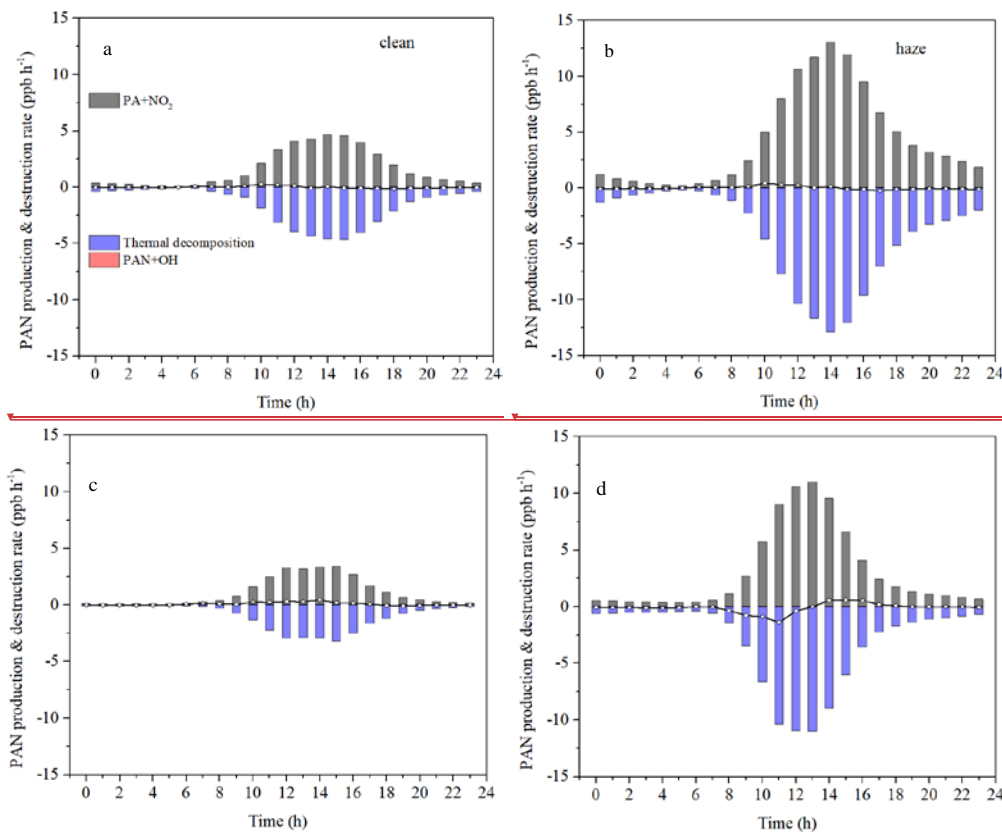
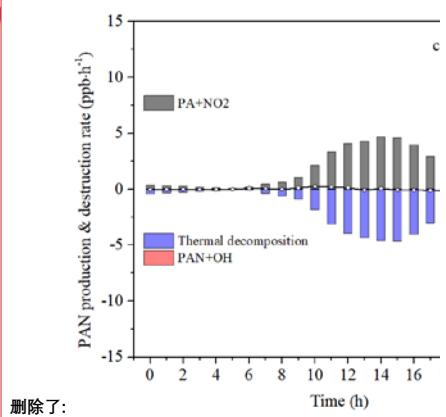
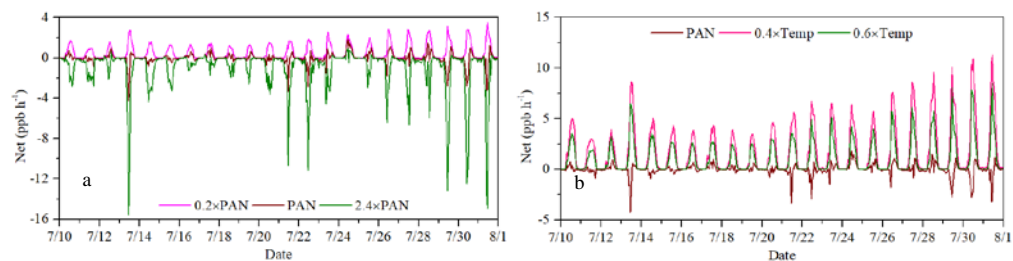
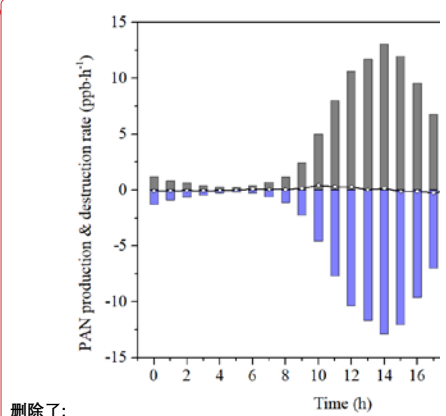


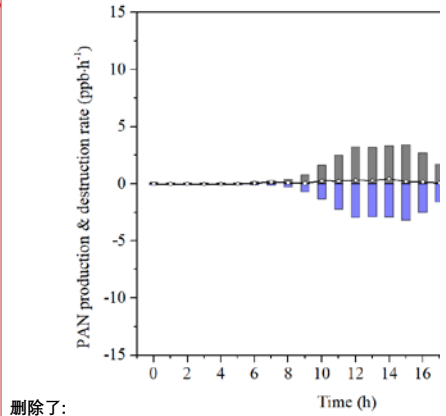
Figure 5. Average diurnal variation of the OBM simulated production, destruction and net rates of PAN during clean (a) and haze (b) days without PAN constrained. And average diurnal variation of the OBM simulated production, destruction and net rates of PAN during clean (c) and haze (d) days with PAN constrained.



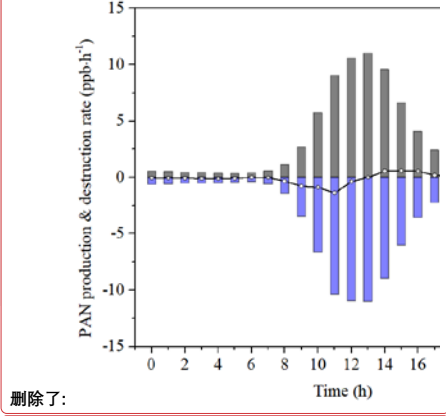
删除了:



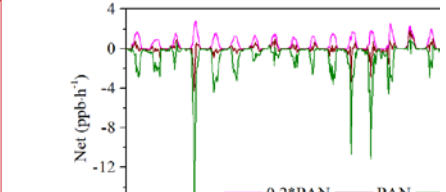
删除了:



删除了:



删除了:



496 **Figure 6.** Net PAN production rates simulated by OBM at different PAN concentrations (a) and different temperatures (b).

497
498 PAN is formed when the PA radical reacts with NO₂. Given the swift equilibrium between R2 and R4 at high temperatures, budget
499 analysis of PA's production and consumption pathways are frequently used to detail the mechanisms behind PAN formation (Sun et
500 al., 2020; Liu et al., 2022a; Liu et al., 2024). Figure 7 illustrates the diurnal patterns of the primary production and loss pathways
501 for the PA radical simulated by OBM across different periods. As shown in Fig. 7, during haze days, the rates of PA production and
502 destruction were twice as high as those on clean days. This indicates that radical cycling and photochemical formation were more
503 efficient during haze days, driven by higher temperatures and a greater abundance of precursors (Zeng et al., 2019). The PA radical
504 production rate from PAN thermal decomposition reached its peak at 15:00 LT (3.22 ppb h⁻¹) and 13:00 LT (10.99 ppb h⁻¹) for clean
505 and haze days, perfectly coinciding with the peak temperature time. In addition, the conversion of PAN into PA radical through
506 thermal decomposition had high exponential correlations with temperature during both haze (R²=0.95) and clean days (R²=0.91)
507 (Fig. S13). Previous laboratory experiments also indicated that the thermal decomposition of PAN is exponentially related to
508 temperature (Cox & Roffey 1977; Senum et al., 1986; Tuazon et al., 1990). The conversion of PAN into PA radical through thermal
509 decomposition during haze days was significantly higher than that during clean days, which was not only enhanced by higher
510 temperature but also maintained by higher PAN concentration during haze days. The thermal decomposition of PAN to PA radical
511 during the day (5:00-18:00 LT) accounted for 68.22 % and 45.59 % during haze and clean days, respectively. The pathways that did
512 not account for the transformation between PA and PAN reached their peak around noon (11:00 LT), coinciding with the highest
513 solar radiation and the most intense photochemical reactions, which has been observed in spring and autumn at the same site (Liu
514 et al., 2022a).

515 Production rates of PA from other pathways related to precursors, including OVOCs, radical cycling, MGLY, and CH₃CHO, showed
516 single-peak patterns around noon, which suggested that the PA radical generated from these pathways was primarily increased by
517 intense solar radiation at noontime (Sun et al., 2020). The average day PA radical production rates from CH₃CHO via reactions with
518 OH and NO₃ were 1.10 and 0.93 ppb h⁻¹, accounting for 48.85 % and 49.35 % (exclude PAN thermal decomposition sources) during
519 haze and clean days, respectively. These percentages were comparable to previous studies in Guangzhou (46 %, Yuan et al., 2018)
520 and Beijing (34.11-50.19 %, Xue et al., 2014), suburban site of Chongqing (47.72 %, Sun et al., 2020). The second production
521 pathway involved MGLY undergoing photolysis and oxidation through reactions with OH and NO₃ (haze: 0.50 ppb h⁻¹ and clean:
522 0.42 ppb h⁻¹), contributing to 22.27 % and 22.12 % for haze and clean days, respectively. Subsequently, radical cycling processes—
523 including the decomposition of RO radicals and the reactions of acyl peroxy radicals with NO—were also significant contributors
524 to PA production, accounting for 18.98 % on haze days and 19.54 % on clean days. PA from the other OVOCs (excluding CH₃CHO,
525 MGLY) via photolysis and oxidation reactions involving OH, NO₃, and O₃, accounted for 9.90 % and 8.99 % during haze (0.22 ppb
526 h⁻¹) and clean days (0.17 ppb h⁻¹). There were no notable differences in the proportions of individual pathways contributing to PA

删除了: .

删除了: .

删除了: local time

删除了: local time

删除了:

删除了: .

删除了:) (

删除了:) (

删除了:) (

删除了: .

删除了: .

删除了: .

删除了: .

between haze and clean days, indicating comparable pollutant compositions in the atmosphere around IUE (Zeng et al., 2019). In summary, the thermal decomposition of PAN played the dominant role in boosting PA production rates during both clean and haze periods, followed by contributions from CH₃CHO, MGLY, radical cycling, and other OVOCs. The primary contributor to the PA destruction rate was the reaction between PA and NO₂, accounting for 67.72 % and 51.09 % during haze (4.74 ppb·h⁻¹) and clean days (1.76 ppb·h⁻¹), respectively, followed by PA+NO, contributing to 32.28 % and 48.91 % during haze (2.26 ppb·h⁻¹) and clean days (1.69 ppb·h⁻¹), respectively.

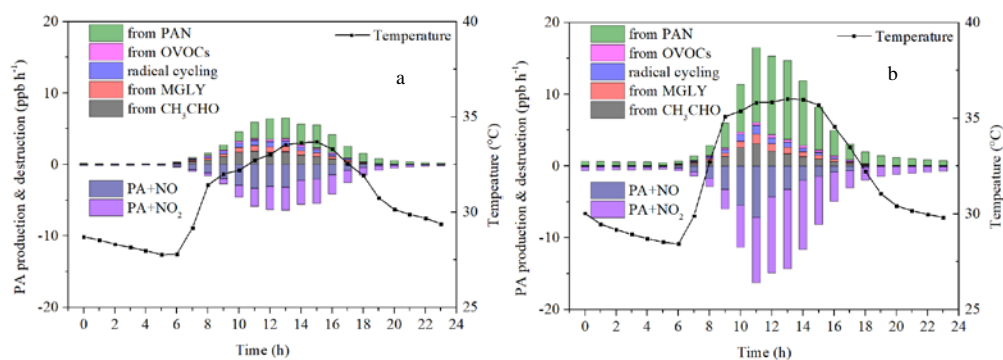


Figure 7. PA radical production and destruction pathways simulated by OBM on (a) clean days and (b) haze days.

3.3 Sensitivity of PAN formation and its impact on the local atmosphere

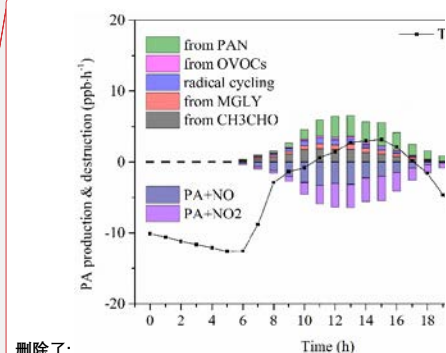
To determine the principal precursors influencing PAN formation, sensitivity modeling analyses were carried out to investigate how PAN relates to its precursors. The RIR reflects how sensitive PAN formation is to changes in its precursor levels. As shown in Fig. 8 (a), the RIR of NO was negative, ranging from -0.67 to -0.27 (-0.52 ± 0.13) throughout the observation period. However, RIR is positive for other species, with NO₂ (0.50 ± 0.11) and VOCs (0.50 ± 0.15) having the highest RIR, followed by HONO (0.12 ± 0.04) and O₃ (0.10 ± 0.03). Around 50 types of VOCs were classified as alkanes, OVOCs, halogenated hydrocarbons (Halo), alkenes, aromatics (Arom), and isoprene (C₅H₈ representing biogenic hydrocarbons). Among these VOCs, the RIR of alkenes (0.22 ± 0.07) is the highest, followed by C₅H₈ (0.13 ± 0.04) and Arom (0.13 ± 0.04), while OVOCs (0.06 ± 0.01) and Halo (0.05 ± 0.01) have very low RIRs (Fig. 8 (b)). These phenomena indicated that increased NO level would inhibit the production of PAN while increased NO₂, VOCs (especially alkenes, C₅H₈, and Arom), HONO, and O₃ would promote the production of PAN. Because the values of NO and NO₂ RIR are approximately equal but with opposite signs, the RIR for NO_x is almost zero, indicating that the PAN generation at this site is not sensitive to NO_x. Zeng et al. (2019) also observed that NO₂ had a positive effect on PAN formation, while NO had a negative effect, in a suburban area of Hong Kong. This finding aligns with the fact that NO₂ directly contributes to PAN production, whereas NO reduces PA radicals, thereby inhibiting PAN formation. Based on the scenario analysis (Empirical Kinetic Modeling Approach (EKMA)), all data points for the 22 days fell above the ridge line (Fig. 8(c)). A reduction

删除了: .

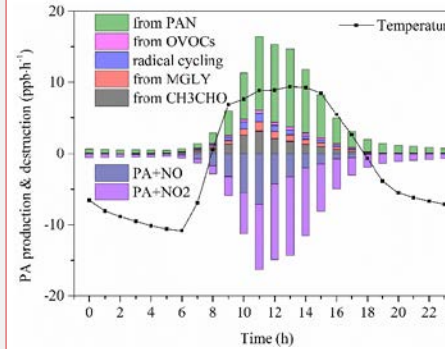
删除了: .

删除了: .

删除了: .



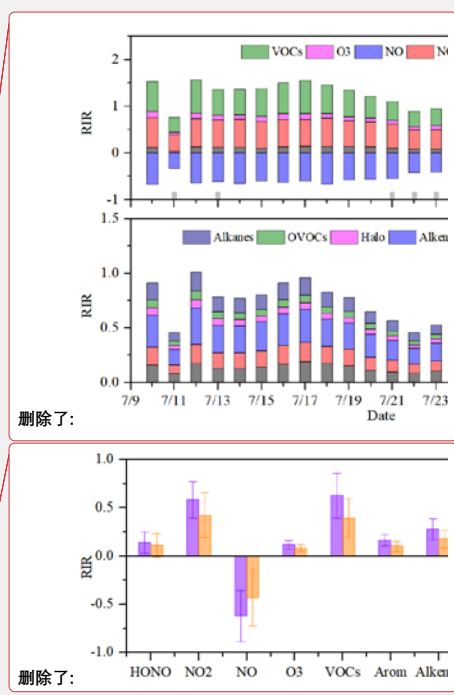
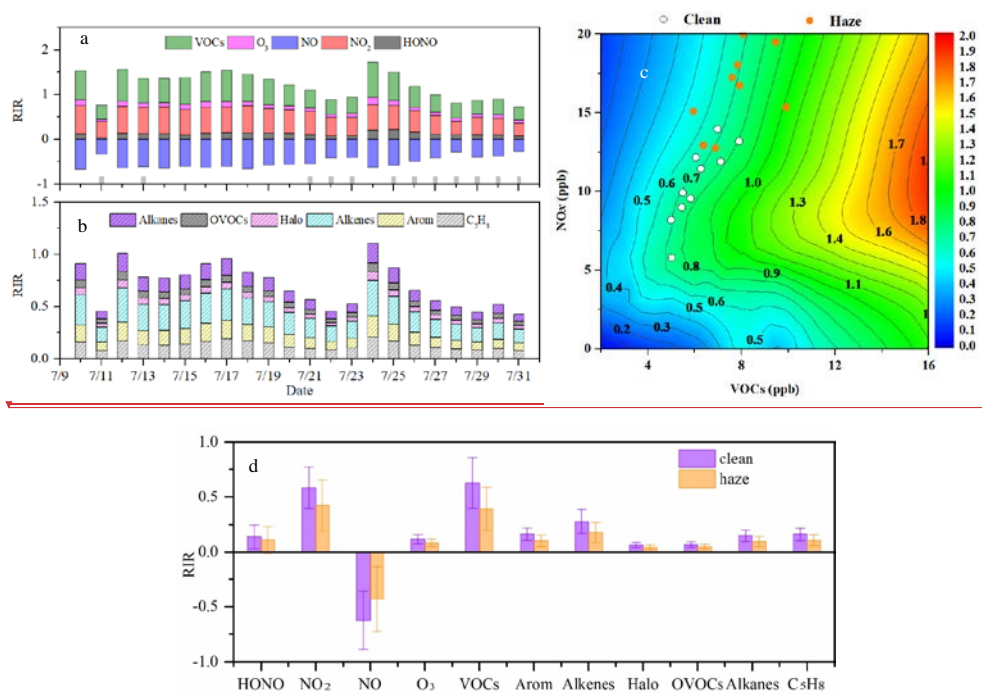
删除了: .



删除了: .

570 in VOCs at these points resulted in lower PAN concentrations, indicating that PAN formation at IUE was influenced by VOCs and
 571 thus VOC-sensitive. Our previous research also found that in this coastal city, PAN generation is limited by VOCs during the
 572 spring and autumn seasons. The difference is that previous studies indicated that reducing NO₂, like reducing NO, also leads to an
 573 increase in PAN concentration in spring and autumn (Liu et al., 2022a). This is because the NO_x concentration in spring and autumn
 574 is significantly higher than in summer, which is consistent with that both NO₂ and NO inhibit the formation of PAN in regions
 575 with high NO_x concentrations (Liu et al., 2024).

576 We divided the RIRs for different species into haze and clean periods and found that the RIRs during clean periods were consistently
 577 higher than those during haze periods (Fig. 8(d)), which indicated that altering the concentrations of these species during clean
 578 periods had a greater impact on PAN formation. The rapid thermal decomposition of PAN at high temperatures is likely the primary
 579 reason. During the haze period, the main source of PA radical was PAN decomposition, which accounted for 68.22%, and the other
 580 sources were smaller than that during the clean period (the source of the PA radical would be demonstrated in the following
 581 paragraph). Therefore, the sensitivity of PAN production to precursors and HONO & O₃ producing OH became lower during the
 582 haze period (Liu et al., 2021b; Liu et al., 2022a).

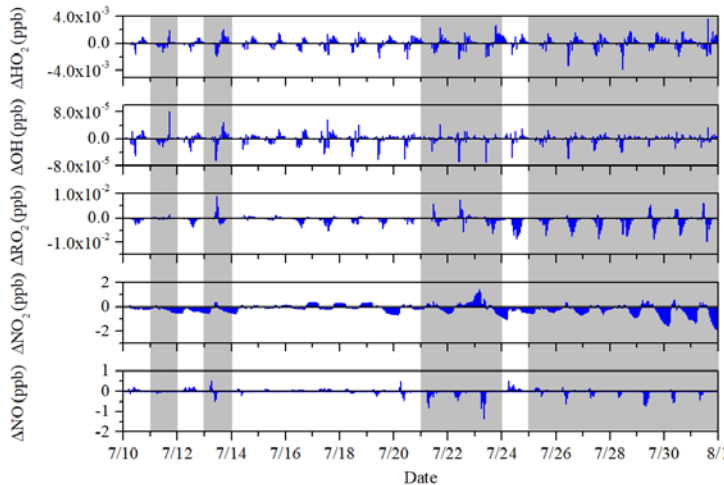


585 **Figure 8.** These four figures illustrate the RIR of PAN formation to major precursors (a), the impact of different VOCs species (b),
 586 the isopleth diagrams of PAN formation (c), and a comparison of RIRs between clean and polluted periods (d).

589
590
591
592
593
594
595
596
597
598
599
600
601
602
603

As shown in Fig. 9, ΔHO_2 and ΔOH are positive for most periods, accounting for 72.16% and 70.83%, respectively, indicating that the PAN mechanism promotes the generation of HO_2 and OH . Over the entire period, ΔHO_2 is $8.43 \cdot 10^{-5}$ ppb, with no significant difference between clean and hazy periods, being $8.18 \cdot 10^{-5}$ ppb and $8.64 \cdot 10^{-5}$ ppb respectively (Table S2). OH behaves similarly, with ΔOH being $4.55 \cdot 10^{-7}$ ppb over the entire period, and also showing no significant difference between clean and hazy periods, being $4.94 \cdot 10^{-7}$ ppb and $4.23 \cdot 10^{-7}$ ppb respectively (Table S2). The increase in simulated OH and HO_2 concentrations suggests that PAN photochemistry is in favor of radical formation and atmospheric oxidative capacity at this site (Liu et al., 2024). Unlike HO_2 and OH , ΔRO_2 and ΔNO_2 are negative for most periods, accounting for 53.22% and 67.23%, respectively, because PAN formation uses up PA and NO_2 , the reduction in PA leads to a decrease in the amount of RO_2 . Over the entire period, ΔRO_2 is $-6.4 \cdot 10^{-4}$ ppb, with no significant difference between clean and hazy periods, being $-6.11 \cdot 10^{-4}$ ppb and $-6.55 \cdot 10^{-4}$ ppb respectively (Table S2). The average value of ΔNO_2 during the entire observation period is -0.17 ppb respectively, with significant differences between hazy and clean periods (Table S2). Specifically, ΔNO_2 is -0.22 during hazy periods and only -0.11 during clean periods, indicating that the PAN mechanism consumes more NO_2 during hazy periods. Although ΔNO is positive for most periods, accounting for 78.79%, the overall mean is -0.01 , with significant differences between hazy and clean periods (Table S2). ΔNO is -0.05 during hazy periods, showing an inhibitory effect, while it is 0.03 during clean periods, showing a promoting effect.

- 删除了: ×
- 删除了: ×
- 删除了: ×
- 删除了: 1
- 删除了: ×
- 删除了: ×
- 删除了: ×
- 删除了: 1
- 删除了: ×
- 删除了: ×
- 删除了: 1
- 删除了: 1
- 删除了: 1

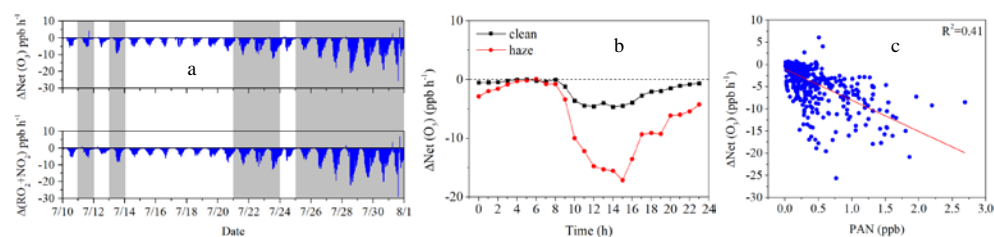


604
605
606
607
608
609

Figure 9. The time series of ΔHO_2 , ΔOH , ΔRO_2 , ΔNO_2 , and ΔNO . The ΔHO_2 , ΔOH , ΔRO_2 , ΔNO_2 , and ΔNO is calculated as the base scenario with the PAN mechanism minus the scenario without the PAN mechanism.

As shown in Fig.10 (a), the PAN mechanism inhibited 85.80% of net O_3 production during the entire observation period, with inhibition rates (the percentage of negative $\Delta\text{Net}(\text{O}_3)$) of 83.75% and 87.50% during clean and haze periods, respectively. This

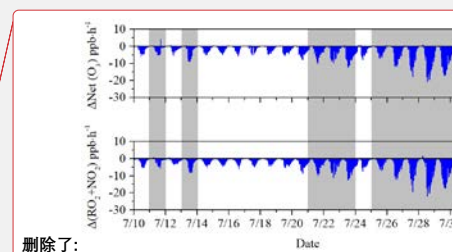
624 result is consistent with previous spring observations at the same site, where the inhibition rate was 83% (Liu et al., 2022a). The
 625 PAN mechanism mainly inhibits the net O₃ generation by increasing the RO₂+NO₂ reaction (Fig.10(a)), with negligible impact from
 626 other reactions (Fig. S14). As shown in Fig.10(b), the diurnal variation trend indicates that the PAN mechanism's inhibitory effect
 627 on O₃ is significantly greater during haze periods than during clean periods. Additionally, regardless of whether it is during haze
 628 periods or clean periods, the PAN mechanism's inhibitory effect on O₃ is significantly greater during the day than at night. These
 629 phenomena all indicate that the higher the PAN concentration, the more pronounced the inhibitory effect of the PAN mechanism on
 630 O₃ (Fig.10(c)). Under the condition of low precursors (including NO_x and VOCs) conditions, competition among these precursors
 631 may limit their secondary transformation, thus resulting in inhibition (Liu et al., 2024).



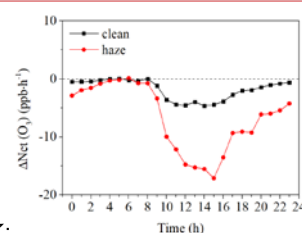
633 **Figure 10.** (a) Time series plot of $\Delta\text{Net}(\text{O}_3)$ and the reaction of $\Delta(\text{RO}_2+\text{NO}_2)$, (b) Diurnal variation of $\Delta\text{Net}(\text{O}_3)$ during clean and
 634 hazy conditions, (c) Correlation between $\Delta\text{Net}(\text{O}_3)$ and PAN. $\Delta\text{Net}(\text{O}_3)$ and $\Delta(\text{RO}_2+\text{NO}_2)$ are calculated as the base scenario with
 635 the PAN mechanism minus the scenario without the PAN mechanism.

637 Conclusion

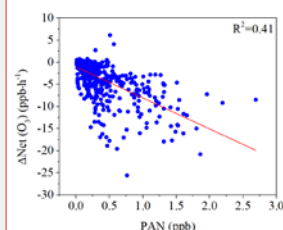
638 This study thoroughly investigated the summertime PAN formation mechanism and established its connection to haze pollution. In
 639 addition to NO and TVOCs, the concentration of all pollutants during the haze period is above twice that during the clean period,
 640 indicating that the oxidation of NO and TVOCs during the haze period is stronger, which is conducive to the oxidation of NO and
 641 TVOCs into secondary pollutants, such as O₃ and PAN. The slopes of linear regression between the daily maximum values of PAN
 642 and O₃ were 0.021 ppb ppb⁻¹ and 0.009 ppb ppb⁻¹ for clean and hazy condition, respectively, implies that PAN precursors accounted
 643 for only a small fraction of the total VOCs, especially for hazy condition. High temperature should be another factor contributing
 644 to the lower production efficiency of PAN in the southeast coastal region. During the whole observation period, the IOA=0.75,
 645 indicating that the MCM model is well-suited for exploring the photochemical formation of PAN. During the clean period,
 646 simulation results were better than during the haze period (R^2 : 0.68 vs. 0.47, slope K: 0.91 vs. 0.75), indicating that some reactions
 647 related to PAN generation or destruction might be missing in the MCM during the hazy period. Additionally, the simulated net
 648 production rate of PAN becomes negative with PAN constrained. However, the observed increase in PAN concentrations indicates
 649 that the actual net production rate is positive, suggesting that there are additional sources contributing to PAN generation that are
 650 not considered in the MCM mechanism. Through XGBoost-SHAP machine learning, and given the significant positive correlation



删除了:



删除了:



删除了: ing

删除了: /

删除了: ppb/ppb

设置了格式: 上标

删除了: increasing

658 between PAN and NO₃⁻ (R= 0.37) at the 0.01 level, and their peak around noon, they likely share a common source. Both RIR and
659 EKMA indicate that PAN formation in this region is VOC-controlled. Controlling emissions of VOCs, particularly alkenes, C₅H₈,
660 and aromatics, would be beneficial for mitigating PAN pollution. The RIR results also show that during the clean period, PAN is
661 more sensitive to changes in various pollutants than during the haze period, highlighting the significant importance of deep emission
662 reductions. PAN presented the promotion effects on OH and HO₂, while inhibited O₃ formation, RO₂, NO and NO₂. This study
663 improves our thorough understanding of PAN photochemistry and offers valuable scientific guidance for the future management of
664 PAN pollution.

665 **Data availability**

666 The observation data at this site are available from the authors upon request.

667 **Authorship Contribution Statement**

668 **Baoye Hu:** Methodology, Formal analysis, Investigation, Data curation, Writing – original draft. **Naihua Chen:** Software, Formal
669 analysis. **Rui Li:** Software, Formal analysis. **Mingqiang Huang:** Software. **Jinsheng Chen:** Funding acquisition, Supervision,
670 Writing - Review & Editing. **Youwei Hong:** Formal analysis. **Lingling Xu:** Investigation. Xiaolong Fan: Investigation. **Mengren**
671 **Li:** Investigation. **Lei Tong:** Investigation. **Qiuping Zheng:** Investigation. **Yuxiang Yang:** Writing - Review & Editing

672 **Competing interests**

673 The authors declare that they have no conflict of interest.

674 **Acknowledgments**

675 This work was supported by the National Natural Science Foundation of China (grant nos. 42305102, U22A20578), the guiding
676 project of seizing the commanding heights of “self-purifying city” (No. IUE-CERAE-202402), Natural Science Foundation of
677 Fujian Province (grant [No.](#) 2023J05179), Natural Science Foundation of Zhangzhou City (grant [No.](#) ZZ2023J07), the Fund of
678 Minnan Normal University President (grant [No.](#) KJ2021009). This study was funded by Xiamen Atmospheric Environment
679 Observation and Research Station of Fujian Province, and Fujian Key Laboratory of Atmospheric Ozone Pollution Prevention
680 (Institute of Urban Environment, Chinese Academy of Sciences).

删除了: nos.

删除了: nos.

设置了格式: 字体: 10 磅

设置了格式: 字体: 10 磅

删除了: nos.

设置了格式: 字体: 10 磅

684 **Supplementary information**

685 Attached please find supplementary information associated with this article.

686 **Reference**

- 687 Behera, S. N., Sharma, M., Aneja, V. P., and Balasubramanian, R.: Ammonia in the atmosphere: a review on emission sources,
688 atmospheric chemistry and deposition on terrestrial bodies, *Environ. Sci. Pollut. Res.*, 20, 8092-8131, 10.1007/s11356-013-
689 2051-9, 2013.
- 690 Cox, R. A., & Roffey, M. J. : Thermal decomposition of peroxyacetylnitrate in the presence of nitric oxide. *Environ. Sci. Tech.*, 11,
691 900-906, 10.1021/es60132a010, 1977.
- 692 Duan, J., Qin, M., Ouyang, B., Fang, W., Li, X., Lu, K., Tang, K., Liang, S., Meng, F., Hu, Z., Xie, P., Liu, W., and Häsel, R.:
693 Development of an incoherent broadband cavity-enhanced absorption spectrometer for in situ measurements of HONO and
694 NO₂, *Atmos. Meas. Tech.*, 11, 4531-4543, 10.5194/amt-11-4531-2018, 2018.
- 695 Hong, Z., Li, M., Wang, H., Xu, L., Hong, Y., Chen, J., Chen, J., Zhang, H., Zhang, Y., Wu, X., Hu, B., and Li, M.: Characteristics
696 of atmospheric volatile organic compounds (VOCs) at a mountainous forest site and two urban sites in the southeast of China,
697 *Sci. Total Environ.*, 657, 1491-1500, 10.1016/j.scitotenv.2018.12.132, 2019.
- 698 Hu, B., Liu, T., Hong, Y., Xu, L., Li, M., Wu, X., Wang, H., Chen, J., and Chen, J.: Characteristics of peroxyacetyl nitrate (PAN) in
699 a coastal city of southeastern China: Photochemical mechanism and pollution process, *Sci. Total Environ.*, 719,
700 10.1016/j.scitotenv.2020.137493, 2020.
- 701 Hu, B., Wang, Y., Chen, J., Chen, N., Hong, Y., Xu, L., Fan, X., Li, M., and Tong, L.: The observation of atmospheric HONO by
702 wet-rotating-denuder ion chromatograph in a coastal city: Performance and influencing factors, *Environ. Pollut.*, 356,
703 10.1016/j.envpol.2024.124355, 2024.
- 704 Hu, B., Duan, J., Hong, Y., Xu, L., Li, M., Bian, Y., Qin, M., Fang, W., Xie, P., and Chen, J.: Exploration of the atmospheric chemistry
705 of nitrous acid in a coastal city of southeastern China: results from measurements across four seasons, *Atmos. Chem. Phys.*,
706 22, 371-393, 10.5194/acp-22-371-2022, 2022.
- 707 Li, H., Yang, Y., Su, H., Wang, H., Wang, P., and Liao, H.: Ozone pollution in China affected by climate change in a carbon neutral
708 future as predicted by a process-based interpretable machine learning method, *Geophys. Res. Lett.*, 51, 10.1029/2024gl109520,
709 2024.
- 710 Lin, Z., Xu, L., Yang, C., Chen, G., Ji, X., Li, L., Zhang, K., Hong, Y., Li, M., Fan, X., Hu, B., Zhang, F., and Chen, J.: Trends of
711 peroxyacetyl nitrate and its impact on ozone over 2018–2022 in urban atmosphere, *Npj Clim. Atmos. Sci.*, 7, 10.1038/s41612-
712 024-00746-7, 2024.

713 Liu, L., Wang, X., Chen, J., Xue, L., Wang, W., Wen, L., Li, D., and Chen, T.: Understanding unusually high levels of peroxyacetyl
714 nitrate (PAN) in winter in Urban Jinan, China, *J. Environ. Sci.*, 71, 249-260, 10.1016/j.jes.2018.05.015, 2018.

715 Liu, T., Chen, G., Chen, J., Xu, L., Li, M., Hong, Y., Chen, Y., Ji, X., Yang, C., Chen, Y., Huang, W., Huang, Q., and Wang, H.:
716 Seasonal characteristics of atmospheric peroxyacetyl nitrate (PAN) in a coastal city of Southeast China: Explanatory factors
717 and photochemical effects, *Atmos. Chem. Phys.*, 22, 4339-4353, 10.5194/acp-22-4339-2022, 2022a.

718 Liu, T., Hong, Y., Li, M., Xu, L., Chen, J., Bian, Y., Yang, C., Dan, Y., Zhang, Y., Xue, L., Zhao, M., Huang, Z., and Wang, H.:
719 Atmospheric oxidation capacity and ozone pollution mechanism in a coastal city of southeastern China: analysis of a typical
720 photochemical episode by an observation-based model, *Atmos. Chem. Phys.*, 22, 2173-2190, 10.5194/acp-22-2173-2022,
721 2022b.

722 Liu, T., Wang, Y., Cai, H., Wang, H., Zhang, C., Chen, J., Dai, Y., Zhao, W., Li, J., Gong, D., Chen, D., Zhai, Y., Zhou, Y., Liao, T.,
723 and Wang, B.: Complexities of peroxyacetyl nitrate photochemistry and its control strategies in contrasting environments in
724 the Pearl River Delta region, *Npj Clim. Atmos. Sci.*, 7, 10.1038/s41612-024-00669-3, 2024.

725 Liu, X., Guo, H., Zeng, L., Lyu, X., Wang, Y., Zeren, Y., Yang, J., Zhang, L., Zhao, S., Li, J., and Zhang, G.: Photochemical ozone
726 pollution in five Chinese megacities in summer 2018, *Sci. Total Environ.*, 801, 149603, 10.1016/j.scitotenv.2021.149603,
727 2021a.

728 Liu, Y., Shen, H., Mu, J., Li, H., Chen, T., Yang, J., Jiang, Y., Zhu, Y., Meng, H., Dong, C., Wang, W., and Xue, L.: Formation of
729 peroxyacetyl nitrate (PAN) and its impact on ozone production in the coastal atmosphere of Qingdao, North China, *Sci. Total
730 Environ.*, 778, 10.1016/j.scitotenv.2021.146265, 2021b.

731 Lu, X., Zhang, L., Wang, X., Gao, M., Li, K., Zhang, Y., Yue, X., and Zhang, Y.: Rapid Increases in Warm-Season Surface Ozone
732 and Resulting Health Impact in China Since 2013, *Environ. Sci. Tech. Lett.*, 7, 240-247, 10.1021/acs.estlett.0c00171, 2020.

733 Marley, N. A., Gaffney, J. S., Ramos-Villegas, R., and ´, B. C. G.: Comparison of measurements of peroxyacetyl nitrates and primary
734 carbonaceous aerosol concentrations in Mexico City determined in 1997 and 2003, *Atmos. Chem. Phys.*, 7, 2277-2285, 2007a.

735 Marley, N. A., Gaffney, J. S., Ramos-Villegas, R., and Gonzalez, B. C.: Comparison of measurements of peroxyacetyl nitrates and
736 primary carbonaceous aerosol concentrations in Mexico City determined in 1997 and 2003, *Atmos. Chem. Phys.*, 7, 2277–
737 2285, 2007b.

738 Pratap, V., Carlton, A. G., Christiansen, A. E., and Hennigan, C. J.: Partitioning of ambient organic gases to inorganic salt solutions:
739 influence of salt identity, ionic strength, and pH, *Geophys. Res. Lett.*, 48, 10.1029/2021gl095247, 2021.

740 Roberts, J. M., Flocke, F., Stroud, C. A., Hereid, D., Williams, E., Fehsenfeld, F., Brune, W., Martinez, M., and Harder, H.: Ground-
741 based measurements of peroxyacetyl nitric anhydrides (PANs) during the 1999 Southern Oxidants Study Nashville
742 Intensive, *J Geophys Res-Atmos*, 107, ACH 1-1-ACH 1-10, 10.1029/2001jd000947, 2002.

743 Senum, G. I., Fajer, R., & Gaffney, J. S. Fourier transform infrared spectroscopic study of the thermal stability of peroxyacetyl

744 nitrate, *J. Phys. Chem.*, 90, 152-156, 10.1021/j100273a034, 1986.

745 Sun, M., Cui, J. n., Zhao, X., and Zhang, J.: Impacts of precursors on peroxyacetyl nitrate (PAN) and relative formation of PAN to
746 ozone in a southwestern megacity of China, *Atmos. Environ.*, 231, 10.1016/j.atmosenv.2020.117542, 2020.

747 Sun, M., Zhou, Y., Wang, Y., Qiao, X., Wang, J., and Zhang, J.: Heterogeneous reaction of peroxyacetyl nitrate on real-world PM_{2.5}
748 aerosols: Kinetics, influencing Factors, and atmospheric implications, *Environ. Sci. Tech.*, 56, 9325-9334,
749 10.1021/acs.est.2c03050, 2022.

750 Taylor, O. C.: Importance of peroxyacetyl nitrate (PAN) as a phytotoxic air pollutant, *J. Air Pollut. Control Assoc.*, 19, 347-351,
751 10.1080/00022470.1969.10466498, 1969.

752 Tuazon, E. C., Carter, W. P., & Atkinson, R. : Thermal decomposition of peroxyacetyl nitrate and reactions of acetyl peroxy radicals
753 with nitric oxide and nitrogen dioxide over the temperature range 283-313 K. *J. Phys. Chem.*, 95, 2434-2437,
754 10.1021/j100159a059, 1991.

755 Wang, B., Shao, M., Roberts, J. M., Yang, G., Yang, F., Hu, M., Zeng, L., Zhang, Y., and Zhang, J.: Ground-based on-line
756 measurements of peroxyacetyl nitrate (PAN) and peroxypropionyl nitrate (PPN) in the Pearl River Delta, China. , *Int. J.*
757 *Environ. Anal. Chem.*, 90, 548–559, 10.1080/03067310903194972, 2010.

758 Wang, H., Lyu, X., Guo, H., Wang, Y., Zou, S., Ling, Z., Wang, X., Jiang, F., Zeren, Y., Pan, W., Huang, X., and Shen, J.: Ozone
759 pollution around a coastal region of South China Sea: interaction between marine and continental air, *Atmos. Chem. Phys.*, 18,
760 4277-4295, 10.5194/acp-18-4277-2018, 2018.

761 Wang, Y., Liu, T., Gong, D., Wang, H., Guo, H., Liao, M., Deng, S., Cai, H., and Wang, B.: Anthropogenic pollutants induce changes
762 in peroxyacetyl nitrate formation intensity and pathways in a mountainous background atmosphere in southern China, *Environ.*
763 *Sci. Tech.*, 10.1021/acs.est.2c02845, 2023.

764 Wu, X., Xu, L., Hong, Y., Chen, J., Qiu, Y., Hu, B., Hong, Z., Zhang, Y., Liu, T., Chen, Y., Bian, Y., Zhao, G., Chen, J., and Li, M.:
765 The air pollution governed by subtropical high in a coastal city in Southeast China: Formation processes and influencing
766 mechanisms, *Sci. Total Environ.*, 692, 1135-1145, 10.1016/j.scitotenv.2019.07.341, 2019.

767 Xu, W., Zhang, G., Wang, Y., Tong, S., Zhang, W., Ma, Z., Lin, W., Kuang, Y., Yin, L., and Xu, X.: Aerosol promotes peroxyacetyl
768 nitrate formation during winter in the North China Plain, *Environ. Sci. Technol.*, 55, 3568-3581, 10.1021/acs.est.0c08157, 2021.

769 Xu, X., Zhang, H., Lin, W., Wang, Y., Xu, W., and Jia, S.: First simultaneous measurements of peroxyacetyl nitrate (PAN) and ozone
770 at Nam Co in the central Tibetan Plateau: impacts from the PBL evolution and transport processes, *Atmos. Chem. Phys.*, 18,
771 5199-5217, 10.5194/acp-18-5199-2018, 2018.

772 Xu, Z., Xue, L., Wang, T., Xia, T., Gao, Y., Louie, P. K. K., and Luk, C. W. Y.: Measurements of peroxyacetyl nitrate at a background
773 site in the Pearl River Delta region: production efficiency and regional transport, *Aerosol Air Qual. Res.*, 15, 833-841,
774 10.4209/aaqr.2014.11.0275, 2015.

775 Xue, L., Wang, T., Wang, X., Blake, D. R., Gao, J., Nie, W., Gao, R., Gao, X., Xu, Z., Ding, A., Huang, Y., Lee, S., Chen, Y., Wang,
776 S., Chai, F., Zhang, Q., and Wang, W.: On the use of an explicit chemical mechanism to dissect peroxy acetyl nitrate formation,
777 *Environ. Pollut.*, 195, 39-47, 10.1016/j.envpol.2014.08.005, 2014.

778 Xue, L. K., Wang, T., Guo, H., Blake, D. R., Tang, J., and Zhang, X. C.: Sources and photochemistry of volatile organic compounds
779 in the remote atmosphere of western China: results from the Mt. Waliguan Observatory, *Atmos. Chem. Phys.*, 13, 8551-8567,
780 10.5194/acp-13-8551-2013, 2013.

781 Yang, X., Wu, K., Wang, H., Liu, Y., Gu, S., Lu, Y., Zhang, X., Hu, Y., Ou, Y., Wang, S., and Wang, Z.: Summertime ozone pollution
782 in Sichuan Basin, China: Meteorological conditions, sources and process analysis, *Atmos. Environ.*, 226,
783 10.1016/j.atmosenv.2020.117392, 2020.

784 Ye, C., Zhang, N., Gao, H., and Zhou, X.: Photolysis of particulate nitrate as a source of HONO and NO_x, *Environ. Sci. Technol.*,
785 51, 6849-6856, 10.1021/acs.est.7b00387, 2017.

786 Yuan, J., Ling, Z., Wang, Z., Lu, X., Fan, S., He, Z., Guo, H., Wang, X., and Wang, N.: PAN-precursor relationship and process
787 analysis of PAN variations in the Pearl River Delta region, *Atmos.*, 9, 10.3390/atmos9100372, 2018.

788 Yukihiro, M., Hiramatsu, T., Bouteau, F., Kadono, T., and Kawano, T.: Peroxyacetyl nitrate-induced oxidative and calcium signaling
789 events leading to cell death in ozone-sensitive tobacco cell-line, *Plant Signal Behav.*, 7, 113-120, 10.4161/psb.7.1.18376, 2012.

790 Zeng, L., Fan, G. J., Lyu, X., Guo, H., Wang, J. L., and Yao, D.: Atmospheric fate of peroxyacetyl nitrate in suburban Hong Kong
791 and its impact on local ozone pollution, *Environ. Pollut.*, 252, 1910-1919, 10.1016/j.envpol.2019.06.004, 2019.

792 Zhai, S., Jacob, D. J., Franco, B., Clarisse, L., Coheur, P., Shah, V., Bates, K. H., Lin, H., Dang, R., Sulprizio, M. P., Huey, L. G.,
793 Moore, F. L., Jaffe, D. A., and Liao, H.: Transpacific transport of Asian peroxyacetyl nitrate (PAN) observed from satellite:
794 implications for ozone, *Environ. Sci. Tech.*, 58, 9760-9769, 10.1021/acs.est.4c01980, 2024.

795 Zhang, G., Mu, Y., Zhou, L., Zhang, C., Zhang, Y., Liu, J., Fang, S., and Yao, B.: Summertime distributions of peroxyacetyl nitrate
796 (PAN) and peroxypropionyl nitrate (PPN) in Beijing: Understanding the sources and major sink of PAN, *Atmos. Environ.*, 103,
797 289-296, 10.1016/j.atmosenv.2014.12.035, 2015.

798 Zhang, J., Guo, Y., Qu, Y., Chen, Y., Yu, R., Xue, C., Yang, R., Zhang, Q., Liu, X., Mu, Y., Wang, J., Ye, C., Zhao, H., Sun, Q., Wang,
799 Z., and An, J.: Effect of potential HONO sources on peroxyacetyl nitrate (PAN) formation in eastern China in winter, *J. Environ.*
800 *Sci. (China)*, 94, 81-87, 10.1016/j.jes.2020.03.039, 2020.

801 Zhang, J. M., Wang, T., Ding, A. J., Zhou, X. H., Xue, L. K., Poon, C. N., Wu, W. S., Gao, J., Zuo, H. C., Chen, J. M., Zhang, X.
802 C., and Fan, S. J.: Continuous measurement of peroxyacetyl nitrate (PAN) in suburban and remote areas of western China,
803 *Atmos. Environ.*, 43, 228-237, 10.1016/j.atmosenv.2008.09.070, 2009.

804 Zhu, J., Wang, S., Wang, H., Jing, S., Lou, S., Saiz-Lopez, A., and Zhou, B.: Observationally constrained modeling of atmospheric
805 oxidation capacity and photochemical reactivity in Shanghai, China, *Atmos. Chem. Phys.*, 20, 1217-1232, 10.5194/acp-20-

806 1217-2020, 2020.

807

808